Preprints of the 21st IFAC World Congress (Virtual)
Berlin, Germany, July 12-17, 2020

Temperature Control for Induction Heating of Thin Strips ⋆,⋆⋆

F. Roetzer * **A. Aschauer** * **L. Jadachowski** ** **A. Steinboeck** *
A. Kugi **,***

* *Automation and Control Institute, TU Wien, Vienna, Austria (e-mail: {roetzer,aschauer,steinboeck}@acin.tuwien.ac.at).*
** *Christian Doppler Laboratory for Model-Based Process Control in the Steel Industry, Automation and Control Institute, TU Wien, Vienna, Austria (e-mail: {jadachowski,kugi}@acin.tuwien.ac.at)*
*** *Center for Vision, Automation & Control, Austrian Institute of Technology, Vienna, Austria (e-mail: andreas.kugi@ait.ac.at)*

Abstract: In this work, a model-based temperature controller for an induction heating system for moving thin metal strips is developed. The most significant disturbance of the system is an uncertain air gap geometry caused by flatness defects of the metal strip. A computationally expensive calculation of the electromagnetic field is avoided by using an equivalent circuit model and the energy balance. A thermal model of the moving strip is derived in the form of a convection-reaction equation and simplified to a linear time-invariant model. A 2-degrees-of-freedom controller is designed based on the simplified model and tested using a finite-element simulation model of the induction heating system. The simulations demonstrate that the proposed controller clearly outperforms standard feedback control strategies.

Keywords: Induction heating, metals industry, temperature control, 2-degrees-of-freedom control

1. INTRODUCTION

Induction heating (IH) is a versatile heating technology for conductive materials because of its high power density, its high energy efficiency, and its capabilities of local reheating. Industrial applications cover the heating, melting, and hardening of rods, slabs, gear wheels, and other parts. As described by Lucía et al. (2014), induction heating systems typically consist of power electronics, magnetic components including the workpiece, and a control system. The controllers applied in this field can be divided into power control, feedforward (FF) control based on magnetic field computations, and temperature control.

Most published control solutions focus on the power supplied to the inductor. The power can be controlled by the amplitude of the supply current, which was shown by Park et al. (2007), Fujita and Akagi (1996), and Egalon et al. (2012). Additionally, Ngoc et al. (2011) eliminated parasitic coupling effects between multiple inductors. For a single inductor system, Zerad et al. (2014) developed a controller that tracks the resonance frequency and thus minimizes the reactive load for the power supply. However, controlling the power supplied to the inductor does not guarantee that the desired heating power enters the workpiece.

One option to capture the difference between the supply power and the actual heating power are magnetic field calculations, which are typically performed by finite-element (FE) software. Pham et al. (2012) and Nguyen et al. (2012) use FE simulations to pre-calculate the distribution of induced currents and utilize these mappings for FF control. These works focus on domestic stoves, where the main objective is homogeneous heating rather than temperature control. Optimal FF temperature control was considered by Rhein and Graichen (2015). The drawback of their approach is that the necessary FE calculations cannot be performed in real time.

With the exception of (Goodwin et al., 2013), the literature lacks reports on feedback (FB) temperature control for industrial IH systems. Goodwin et al. (2013) designed a nonlinear model predictive controller based on a finite-difference model of a cylindrical rod with a surrounding coil. In this scenario, changes of the air gap geometry due to an excentric rod position are practically negligible.

The current paper focuses on IH of moving, thin, paramagnetic strips with uncertain flatness defects. Therefore, the impact of a time-varying air gap between the strip and the inductor is investigated in detail. For pure FF control, a highly accurate and detailed process model would be required. To avoid this, a 2-degrees-of-freedom (2DOF) control structure is designed, where the FB loop facilitates the use of a simpler process model for the FF controller despite the uncertain air gap width. A central objective of

⋆ This work has been performed in the project Power Semiconductor and Electronics Manufacturing 4.0 (SemI40), under grant agreement No 692466. The project is co-funded by grants from Austria, Germany, Italy, France, Portugal and the Electronic Component Systems for European Leadership Joint Undertaking (ECSEL JU).
⋆⋆The financial support by the Christian Doppler Research Association, the Austrian Federal Ministry for Digital and Economic Affairs, and the National Foundation for Research, Technology and Development is gratefully acknowledged.

the current work is to develop a reliable, computationally undemanding, and easy-to-use control strategy.

The paper is structured as follows. In Section 2, the considered system is described and a detailed FE model is developed. The model undergoes a number of simplifications in Section 3 to obtain a control-oriented computationally undemanding model. Based on this model, a 2DOF controller structure is designed in Section 4. Numerical results are shown in Section 5 and final remarks are given in Section 6.

2. PROCESS MODEL

The considered IH system is used by Plansee SE (Reutte, Austria) to reheat molybdenum strips and is outlined in Fig. 1. A thin molybdenum strip (domain $\Omega^p \subset \mathbb{R}^3$, boundary $\partial\Omega^p$) moves under a longitudinal inductor coil winding (domain $\Omega^c \subset \mathbb{R}^3$ for the conductor). In this way, a narrow stripe of the metal strip is reheated. Along this stripe, a downstream slitting shear cuts the strip. The quality of the cutting edge depends on the strip temperature.

The metal strip Ω^p has a thickness of l_y and moves with the constant velocity v_x along the direction x. Because of residual stresses generated during an upstream rolling process, the strip exhibits uncertain flatness defects. For the IH process, the resulting non-zero curvature in the x-y plane is relevant insofar as it entails an uncertain and time-variant air gap width $a^{\mathrm{g}}(x,t)$. The strip entry temperature $T^{\mathrm{in}}(t)$ and the exit temperature $T^{\mathrm{out}}(t)$ are measured by pyrometers on the upper surface at the points $[x,z]{=}[0,0]$ and $[x,z]{=}[l_x,0]$, respectively. Throughout Ω^p, the commonly observed temperature non-uniformities cause only insignificant thermal stresses.

The winding Ω^c is a hollow conductor with rectangular cross-section and internal water cooling. Magnetic cores of width l_z enclose the conductor and guide the magnetic flux. The coil reaches from $x{=}\Delta l$ to $x{=}l_x{-}\Delta l$.

The inductor is part of a parallel resonant circuit with a capacitor C^{r}. The capacitor and the inductor are coupled by an ideal transformer with the ratio $1{:}a^{\mathrm{t}}$. The resonant circuit is driven by an AC voltage source with adjustible RMS voltage U^{s} and angular frequency ω. The RMS voltage U^{s} and the RMS current I^{s} at the voltage source and the RMS current I through the inductor are known from measurements.

The goal of the temperature controller is to heat the metal strip to the desired value $T_d^{\mathrm{out}}(t)$ with a tolerance of $\pm 50°\mathrm{C}$ at the center of the stripe ($z{=}0$). The time-varying air gap $a^{\mathrm{g}}(x,t)$ is an unknown disturbance.

As a basis for all further derivations, a 3D FE model of the magnetic field is formulated and implemented in COMSOL MULTIPHYSICS.

2.1 Electromagnetic Field

Consider Maxwell's equations for the dominant-magnetic case, i.e., electrostatic charges and changes of the electric displacement field are neglected. With the magnetic field $\boldsymbol{H}$, the magnetic flux density $\boldsymbol{B}$, the electric field $\boldsymbol{E}$, and the current density $\boldsymbol{J}$, Maxwell's equations have the form

$$\boldsymbol{\nabla} \times \boldsymbol{H} = \boldsymbol{J}, \quad \boldsymbol{\nabla} \times \boldsymbol{E} = -\partial_t \boldsymbol{B}, \quad \boldsymbol{\nabla} \cdot \boldsymbol{B} = 0. \tag{1}$$

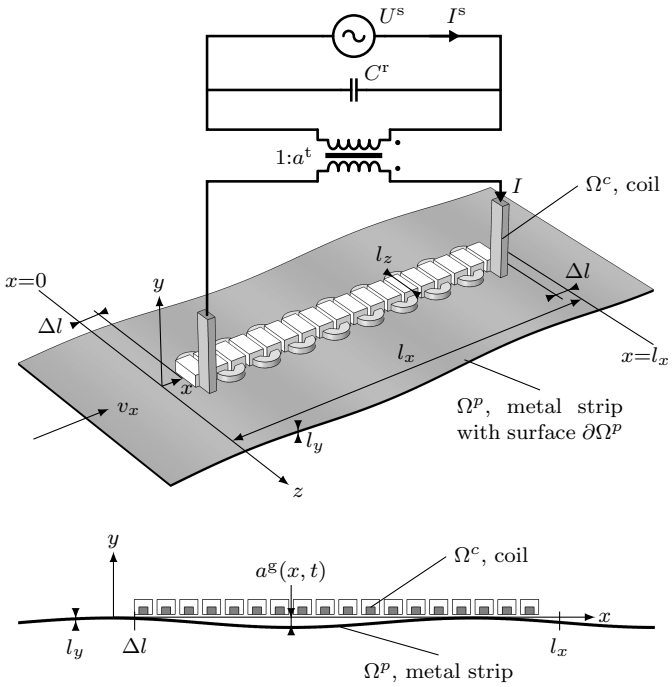

Fig. 1. IH system: Inductor coil and plate geometries as parts of a resonant circuit.

The associated constitutive equations are [1]

$$\boldsymbol{B} = \mu \boldsymbol{H}, \quad \boldsymbol{J} = \sigma \boldsymbol{E}, \tag{2}$$

where μ and σ are the magnetic permeability and the electric conductivity, respectively. Initial and boundary conditions are appropriately chosen.

Using the magnetic vector potential $\boldsymbol{A}$ defined in the form

$$\boldsymbol{B} = \boldsymbol{\nabla} \times \boldsymbol{A}, \tag{3}$$

(1) and (2) can be consolidated into (cf. Jackson (2011))

$$\boldsymbol{\nabla} \times (\mu^{-1} \boldsymbol{\nabla} \times \boldsymbol{A}) = \boldsymbol{J} = \begin{cases} \boldsymbol{J}^{\mathrm{c}}(I), & \Omega^c \\ -\sigma \partial_t \boldsymbol{A}, & \text{else.} \end{cases} \tag{4}$$

$\boldsymbol{J}^{\mathrm{c}}(I)$ is the current density in the conductor, depending on the externally controlled current I. The term $-\sigma\partial_t \boldsymbol{A}$ represents the induced current density in the remaining volume. If induction takes place inside Ω^c, the two cases of (4) are mixed accordingly.

For IH, it is sufficient to consider time-harmonic solutions of the electromagnetic system. Therefore, the harmonic formulations $\boldsymbol{A}{=}\mathrm{Re}\left(\hat{\boldsymbol{A}} e^{j\omega t}\right)$ and $\boldsymbol{J}^{\mathrm{c}}{=}\mathrm{Re}\left(\hat{\boldsymbol{J}}^{\mathrm{c}} e^{j\omega t}\right)$, with the imaginary unit j and the complex amplitudes $\hat{\boldsymbol{A}}$ and $\hat{\boldsymbol{J}}^{\mathrm{c}}$, are used. The steady-state version of (4) is thus

$$\boldsymbol{\nabla} \times (\mu^{-1} \boldsymbol{\nabla} \times \hat{\boldsymbol{A}}) = \begin{cases} \hat{\boldsymbol{J}}^{\mathrm{c}}, & \Omega^c \\ -j\omega\sigma \hat{\boldsymbol{A}}, & \text{else,} \end{cases} \tag{5}$$

again with appropriate boundary conditions.

For the remainder of this paper, the time scale of the electromagnetic field problem is considered several orders of magnitude faster than the heat transfer dynamics. Thus, all time dependencies of the electromagnetic quantities are

[1] In case of a ferromagnetic strip, a nonlinear material law B(H), cf. (2), has to be considered in (1). In this context, an in-line estimation approach is proposed by Jadachowski et al. (2020).

considered on the larger time scale of the heat transfer problem.

2.2 Heat Transfer

Due to the cooling water in the hollow conductor, all material points outside the strip domain Ω^p are assumed to have a constant uniform temperature. Heat transfer is thus considered in the domain Ω^p. For this domain, the heat conduction equation with advection due to the strip movement along the x direction and the heating due to IH reads as (cf. Incropera et al., 2007)

$$\rho c_p(\partial_t T + v_x \partial_x T) = \boldsymbol{\nabla} \cdot (\lambda \boldsymbol{\nabla} T) + \frac{\sigma\omega^2}{2}\|\hat{\boldsymbol{A}}\|_2^2. \quad (6a)$$

Here, T, ρ, c_p, and λ denote the temperature, mass density, specific heat capacity, and thermal conductivity of the strip, respectively.

Each material point of the strip stays in the magnetic field domain only for a few seconds. Due to this short time span, the losses due to radiative and convective cooling on $\partial\Omega^p$ are neglected. Using the derivative operator ∂_n along the surface normal direction, (6a) is supplemented by the boundary conditions

$$T - T^{\text{in}} = 0, \qquad x = 0, \quad (6b)$$
$$-\lambda \partial_n T = 0, \qquad \text{on } \partial\Omega^p, \quad (6c)$$

and by the initial condition $T{=}T_0$ at $t{=}0$.

2.3 Implementation and Validation

The model (5) and (6) was implemented in COMSOL MULTIPHYSICS. For validation of the model, a heating experiment was conducted at the industrial plant and the obtained time-averaged measurement values were compared to the results of the model for a quasi-stationary scenario.

Experiment. The signals ω, U^{s}, I^{s}, T^{in}, T^{out}, and a^{g} were recorded and their time averages $\overline{\omega}$, $\overline{U}^{\text{s}}$, $\overline{I}^{\text{s}}$, $\overline{T}^{\text{in}}$, $\overline{T}^{\text{out}}$, and $\overline{a}^{\text{g}}$, respectively, were computed. These time averages are given in Table 1. Due to the low temperatures, the pyrometer readings T^{in} and T^{out} are sensitive to disturbances. The mean air gap $\overline{a}^{\text{g}}$ was extracted from video data using the CANNY algorithm (cf. Canny, 1986).

Table 1. Data from the heating experiment.

Quantity	Magnitude	Max. uncertainty
$\overline{\omega}$	$2\pi \times 7746\,\text{rad}\,\text{s}^{-1}$	$\pm 2\pi \times 10\,\text{rad}\,\text{s}^{-1}$
$\overline{U}^{\text{s}}$	679.5V	±0.5V
$\overline{I}^{\text{s}}$	150.7A	±0.1A
$\overline{T}^{\text{in}}$	30°C	±5°C
$\overline{T}^{\text{out}}$	268°C	±5°C
$\overline{a}^{\text{g}}$	8.4mm	±0.5mm
v_x	$0.1\,\text{m}\,\text{s}^{-1}$	$\pm 0.01\,\text{m}\,\text{s}^{-1}$

In these experiments, the current I entering the inductor (cf. Fig. 1) and the phase angles of U^{s} and I^{s} were not measured. The transformer ratio $1{:}a^{\text{t}}$ is also not known exactly. These missing quantities were estimated before the simulation model was evaluated. For this purpose, the following inverse problem was solved.

Inverse problem. The complex power S^{s} supplied by the voltage source is distributed to the capacitor and the inductor, i.e., $S^{\text{s}}{=}S(I){-}j\omega C^{\text{r}}\,|U^{\text{s}}|^2$. $S(I)$ is the complex power supplied to the inductor and can be computed by the FE model. To compute the inductor current I, the inverse problem

$$\min_I \left(\left| \overline{U}^{\text{s}} \overline{I}^{\text{s}} \right| - \left| S(I) - j\overline{\omega} C^{\text{r}} |\overline{U}^{\text{s}}|^2 \right| \right)^2, \quad \text{s.t. } \omega = \overline{\omega} \quad (7)$$

is solved using the algorithm SNOPT (cf. Gill et al., 2005).

Model validation. At the steady state, the process model yields the exit temperature

$$T^{\text{out}} = 290°\text{C}. \quad (8)$$

Based on the solution of (7), the sensitivity

$$\left.\frac{\partial T^{\text{out}}}{\partial a^{\text{g}}}\right|_{a^{\text{g}}=\overline{a}^{\text{g}}} \approx -86°\text{C}\,\text{mm}^{-1} \quad (9)$$

of T^{out} with respect to a^{g} was calculated by finite differences. With the given uncertainty of 0.5mm for $\overline{a}^{\text{g}}$, it holds that

$$\big|\underbrace{T^{\text{out}}}_{(8)} - \underbrace{\overline{T}^{\text{out}}}_{\text{Table 1}}\big| = 22°\text{C} < \underbrace{86°\text{C}\,\text{mm}^{-1}}_{(9)} \times \underbrace{0.5\text{mm}}_{\text{Table 1}}. \quad (10)$$

This implies that the FE model is within the uncertainties of the given measurement data and thus conforms to the recorded measurements.

The validated 3D FE model is mainly used to evaluate the performance of the proposed controller by simulations.

3. CONTROL-ORIENTED MODEL

Based on the process model (5) together with (6), a reduced model suitable for real-time control is derived for controller design.

3.1 Reduction to a 2D Problem

Using the specific enthalpy

$$h(x,y,z,t) = \int_0^{T(x,y,z,t)} \rho c_p(T')\mathrm{d}T', \quad (11)$$

(6) can be rewritten in the form

$$\partial_t h + v_x \partial_x h = \boldsymbol{\nabla} \cdot \left(\frac{\lambda}{\rho c_p} \boldsymbol{\nabla} h \right) + \frac{\sigma\omega^2}{2}\|\hat{\boldsymbol{A}}\|_2^2, \quad (12a)$$

with the boundary and initial conditions

$$h(0,y,z,t) = h^{\text{in}}(t) \quad (12b)$$
$$\partial_n h(x,y,z,t) = 0, \qquad \text{on } \partial\Omega^p, x \neq 0 \quad (12c)$$
$$h(x,y,z,0) = h_0(x,y,z). \quad (12d)$$

Simulations show that the convective term $v_x\partial_x h$ in (12a) dominates the heat transfer along the x direction. Conduction contributes only 4% to the longitudinal heat transfer and is therefore neglected. Along the lateral direction z, however, there is no motion of the strip and conductive heat transfer is relevant. The lateral heat flux will be denoted by $\dot{q}_z{=}-\frac{\lambda}{\rho c_p}\partial_z h$.

Furthermore, stray magnetic fields along the z direction will be neglected. Hence, the calculation domain can be limited to the stripe $|z|{<}l_z/2$ and $\hat{\boldsymbol{A}}$ can be considered as independent of z. Finally, examining isothermal surfaces in the 3D model shows that the assumption of a uniform

strip temperature T along the thickness direction y is reasonable.

With these simplifications, (12a) reduces to

$$\partial_t \overline{h}(x,t) + v_x \partial_x \overline{h}(x,t) = \overline{\frac{\sigma\omega^2}{2}\|\hat{\boldsymbol{A}}\|_2^2} - \frac{1}{l_z}\dot{q}_z\big|_{z=-\frac{l_z}{2}}^{z=\frac{l_z}{2}}, \quad x \in (0, l_x), t > 0, \tag{13}$$

where $\overline{h}$ and $\overline{\frac{\sigma\omega^2}{2}\|\hat{\boldsymbol{A}}\|_2^2}$ denote mean values over the cross-section of the stripe $|z|<l_z/2$. The boundary and initial conditions likewise transform into

$$\overline{h}(0,t) = \overline{h}^{\mathrm{in}}(t), \quad \overline{h}(x,0) = \overline{h}_0(x). \tag{14}$$

3.2 Equivalent Circuit Formulation

In order to further simplify the right-hand side of (13), consider the equivalent circuit diagram shown in Fig. 2. This is a lumped-parameter approximation of the electromagnetic field problem (5).

The ohmic losses in the conductor Ω^{c} and the strip Ω^{p} are represented by the resistors R^{c} and R^{p}, respectively. The inductors L_σ^c and L_σ^p describe the stray magnetic flux, while L_h describes the coupling between the coil and the strip. The resistor R^{Fe} accounts for losses in the magnetic cores.

The active electrical power P=Re $(S(I))$ supplied to the coil can only be dissipated by the resistors. Hence, P can be split into

$$P(t) = R^c |I(t)|^2 + P^p(t) + P^l(t), \tag{15}$$

where P^p is the power that effectively heats the stripe in the area $|z|<l_z/2$. Other losses in the magnetic core and due to lateral heat diffusion $\dot{q}_z$, or gains due to proximity effects, are summarized in the term $P^l(t)$. Therefore,

$$\overline{\frac{\sigma\omega^2}{2}\|\hat{\boldsymbol{A}}\|_2^2} - \frac{1}{l_z}\dot{q}_z\big|_{z=-\frac{l_z}{2}}^{z=\frac{l_z}{2}} = b(x,t)P^p(t) \tag{16}$$

can be substituted for the right-hand side of (13). The function $b(x,t)$ has the unit m^{-3} and describes the spatial distribution of the heating power P^p along x. It must be obtained from measurements, calculation, or estimation. Energy conservation for the domain Ω^{p} requires

$$\forall t > 0 : l_y l_z \int_0^{l_x} b(x,t)\mathrm{d}x \equiv 1. \tag{17}$$

Insertion of (16) into (13) and consideration of (15) yields the control-oriented model

$$\partial_t \overline{h}(x,t) + v_x \partial_x \overline{h}(x,t) = b(x,t)\left(P(t) - R^c|I(t)|^2 - P^l(t)\right), \tag{18}$$

with (14) and the output equation

$$\overline{h}^{\mathrm{out}}(t) = \overline{h}(l_x,t) + n(t). \tag{19}$$

The term $n(t)$ represents the pyrometer measurement noise at x=l_x. For the unknown power loss P^l, the disturbance model

$$\frac{\mathrm{d}}{\mathrm{d}t}P^l(t) = w(t), \quad P^l(0) = P_0^l, \tag{20}$$

with the process noise $w(t)$, is formulated.

The control-oriented model (18), (14), (19) does not contain any material parameters of the strip. Transformations between the specific enthalpy and the temperature based on (11) can be done outside of the control loop. The power losses $P^l(t)$ have to be estimated in real time.

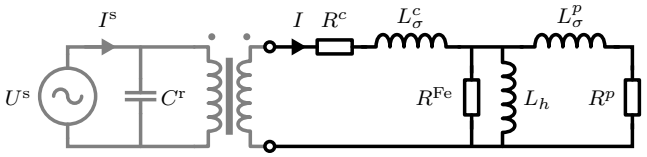

Fig. 2. Equivalent circuit diagram of the IH system.

3.3 Discretization

The control-oriented model (18), (14), (19), and (20) is discretized in space and time using the finite volume method and the upwind scheme. Let the uniform spatial step size be Δx=l_x/N and the constant sampling time Δt. They have to satisfy the Courant-Friedrichs-Lewy condition (cf. Courant et al. (1928)) C=$\frac{v_x \Delta t}{\Delta x} \leq 1$. This yields the discrete-time model

$$\begin{bmatrix} \boldsymbol{h}_{k+1} \\ P_{k+1}^l \end{bmatrix} = \begin{bmatrix} \boldsymbol{\Phi} & -\boldsymbol{\Gamma}_k \\ \boldsymbol{0}^{\mathrm{T}} & 1 \end{bmatrix} \begin{bmatrix} \boldsymbol{h}_k \\ P_k^l \end{bmatrix} + \begin{bmatrix} \boldsymbol{\Gamma}_k & \boldsymbol{\Gamma}^{\mathrm{in}} \\ 0 & 0 \end{bmatrix} \begin{bmatrix} u_k \\ h_k^{\mathrm{in}} \end{bmatrix} + \begin{bmatrix} \boldsymbol{0} \\ \Delta t \end{bmatrix} w_k \tag{21a}$$

$$y_k = \boldsymbol{c}^{\mathrm{T}} \boldsymbol{h}_k + n_k, \tag{21b}$$

with the state vector

$$\boldsymbol{h}_k = [\overline{h}(j\Delta x, k\Delta t)]_{j=1,\ldots,N}, \tag{22a}$$

the system matrices

$$\boldsymbol{\Phi} = \begin{bmatrix} 1-C & 0 & 0 & \ldots \\ C & 1-C & 0 & \ldots \\ 0 & C & 1-C & \ldots \\ \vdots & \vdots & \vdots & \ddots \end{bmatrix}, \tag{22b}$$

$$\boldsymbol{\Gamma}_k = \left[\frac{\Delta t}{\Delta x} \int_{(j-1)\Delta x}^{j\Delta x} b(x, k\Delta t)\mathrm{d}x \right]_{j=1,\ldots,N}, \tag{22c}$$

$$\boldsymbol{\Gamma}^{\mathrm{in}} = [C \ 0 \ 0 \ \ldots]^{\mathrm{T}}, \tag{22d}$$

$$\boldsymbol{c}^{\mathrm{T}} = [0 \ \ldots \ 0 \ 1], \tag{22e}$$

and the signals

$$u_k = P(k\Delta t) - R^c |I(k\Delta t)|^2,$$
$$P_k^l = P^l(k\Delta t), \quad w_k = w(k\Delta t), \quad h_k^{\mathrm{in}} = \overline{h}^{\mathrm{in}}(k\Delta t),$$
$$y_k = \overline{h}^{\mathrm{out}}(k\Delta t), \quad n_k = n(k\Delta t). \tag{22f}$$

To validate the reduced control-oriented model (21), Fig. 3 shows the response of T^{out} to a step change of the input I, which corresponds to a step change in P, computed by both the FE model (6) and the control-oriented model (21). For this scenario, a homogeneous air gap a^{g} is chosen, and for the distribution $b(x,t)$ of the heating power $P^p(t)$

$$b(x,t) = \begin{cases} ((l_x - 2\Delta l) l_y l_z)^{-1} & \Delta l < x < l_x - \Delta l \\ 0 & \text{else.} \end{cases} \tag{23}$$

The parameter values are taken from Table 1. For the power losses P_0^l=2kW is used, for the process noise w_k=0, and for the measurement noise n_k=0.

4. TEMPERATURE CONTROL

The unknown distribution $b(x,t)$ is assumed as in (23). Consequently

$$\boldsymbol{\Gamma}_k = \boldsymbol{\Gamma} = \text{const.}, \tag{24}$$

and (21) becomes a linear, time-invariant (LTI) model.

For output tracking control, the 2DOF controller structure shown in Fig. 4 is designed.

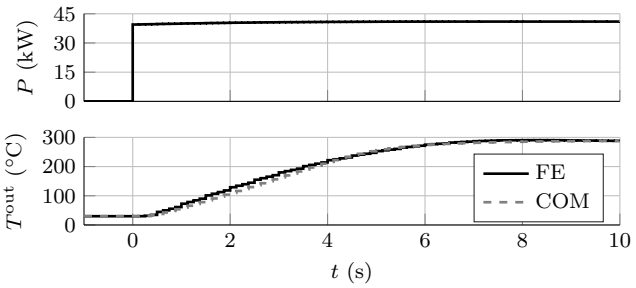

Fig. 3. Step responses of the 3D FE model and the control-oriented model (COM) for $a^g(x,t)$=const.

4.1 Feedforward Controller

From (21) and (24), the disturbance-free (P_k^l=0, w_k=0, n_k=0) LTI FF model reads as

$$\boldsymbol{h}_{k+1}^{\mathrm{ff}} = \boldsymbol{\Phi}\boldsymbol{h}_k^{\mathrm{ff}} + \boldsymbol{\Gamma}u_k^{\mathrm{ff}} + \boldsymbol{\Gamma}^{\mathrm{in}}h_k^{\mathrm{in}} \tag{25a}$$

$$y_k^{\mathrm{ff}} = \boldsymbol{c}^{\mathrm{T}}\boldsymbol{h}_k^{\mathrm{ff}} \tag{25b}$$

with the initial condition $\boldsymbol{h}_0^{\mathrm{ff}} = \boldsymbol{h}_0$.

The input-output representation of (25) can be written as

$$y_k^{\mathrm{ff}} = G_{uy}(\delta)u_k^{\mathrm{ff}} + \underbrace{\boldsymbol{c}^{\mathrm{T}}\left(\delta\boldsymbol{I}-\boldsymbol{\Phi}\right)^{-1}\left(\boldsymbol{h}_0\delta_0 + \boldsymbol{\Gamma}^{\mathrm{in}}h_k^{\mathrm{in}}\right)}_{=y_k^0}, \tag{26}$$

with the forward time shift operator δ for one sampling interval, the discrete-time impulse δ_0, the identity matrix $\boldsymbol{I}$, and the transfer function operator from u_k^{ff} to y_k^{ff}

$$G_{uy}(\delta) = \boldsymbol{c}^{\mathrm{T}}\left(\delta\boldsymbol{I}-\boldsymbol{\Phi}\right)^{-1}\boldsymbol{\Gamma}. \tag{27}$$

Choosing y_k^{ff} equal to the desired output $y_{d,k}$ and assuming a stationary specific input enthalpy h_k^{in}=h_s^{in} and $\boldsymbol{h}_0$=$\mathbf{1}h_s^{\mathrm{in}}$, such that y_k^0=h_s^{in}, yields the FF control law

$$u_k^{\mathrm{ff}} = G_{uy}^{-1}(\delta)\left(y_{d,k} - h_s^{\mathrm{in}}\right). \tag{28}$$

Although $G_{uy}^{-1}(\delta)$ is not proper [2], the FF controller (28) can be realized because the reference input $y_{d,k}$ is known for a sufficient time in advance.

The error y_k^{fb}=y_k−$y_{d,k}$ is passed to a FB controller, which is designed in the following steps.

4.2 Feedback Controller

Let $\boldsymbol{h}_k^{\mathrm{fb}}$=$\boldsymbol{h}_k - \boldsymbol{h}_k^{\mathrm{ff}}$ and u_k^{fb}=$u_k - u_k^{\mathrm{ff}}$. The task of the FB controller is to control the output y_k^{fb} of the error system

$$\begin{bmatrix}\boldsymbol{h}_{k+1}^{\mathrm{fb}}\\ P_{k+1}^l\end{bmatrix} = \begin{bmatrix}\boldsymbol{\Phi} & -\boldsymbol{\Gamma}\\ \mathbf{0}^{\mathrm{T}} & 1\end{bmatrix}\begin{bmatrix}\boldsymbol{h}_k^{\mathrm{fb}}\\ P_k^l\end{bmatrix} + \begin{bmatrix}\boldsymbol{\Gamma}\\ 0\end{bmatrix}u_k^{\mathrm{fb}} + \begin{bmatrix}\mathbf{0}\\ \Delta t\end{bmatrix}w_k \tag{29a}$$

$$y_k^{\mathrm{fb}} = \boldsymbol{c}^{\mathrm{T}}\boldsymbol{h}_k^{\mathrm{fb}} + n_k, \tag{29b}$$

with the initial condition $\boldsymbol{h}_0^{\mathrm{fb}} = \mathbf{0}$.

For (29), a linear-quadratic Gaussian (LQG) controller consisting of a Kalman filter (KF) observer and a linear-quadratic regulator (LQR) will be designed.

Observer. The observability of (29) can be easily proven by an eigenvector test. For the design of a KF for (29), let $\hat{\boldsymbol{x}}_k^e$=$[(\hat{\boldsymbol{h}}_k^{\mathrm{fb}})^{\mathrm{T}}, \hat{P}_k^l]^{\mathrm{T}}$ be the estimated values of $\boldsymbol{h}_k^{\mathrm{fb}}$ and P_k^l. With

$$\boldsymbol{\Phi}^e = \begin{bmatrix}\boldsymbol{\Phi} & -\boldsymbol{\Gamma}\\ \mathbf{0}^{\mathrm{T}} & 1\end{bmatrix},\ \boldsymbol{\Gamma}^e = \begin{bmatrix}\boldsymbol{\Gamma}\\ 0\end{bmatrix},\ \boldsymbol{G}^e = \begin{bmatrix}\mathbf{0}\\ \Delta t\end{bmatrix},\ \boldsymbol{c}^e = \begin{bmatrix}\boldsymbol{c}\\ 0\end{bmatrix},$$

$$Q^e = \mathrm{cov}\left(w_k\right) = (1\mathrm{W\,s^{-1}})^2,$$

$$R^e = \mathrm{cov}\left(n_k\right) = (3.16\times10^4\mathrm{J\,m^{-3}})^2, \tag{30}$$

the steady-state KF reads as

$$\hat{\boldsymbol{x}}_{k+1}^e = \boldsymbol{\Phi}^e\hat{\boldsymbol{x}}_k^e + \boldsymbol{\Gamma}^e u_k^{\mathrm{fb}} + \hat{\boldsymbol{K}}^e(y_k^{\mathrm{fb}} - (\boldsymbol{c}^e)^{\mathrm{T}}\hat{\boldsymbol{x}}_k^e). \tag{31}$$

The gain vector $\hat{\boldsymbol{K}}^e$ follows from the algebraic Riccati equation

$$\boldsymbol{P}^e = \boldsymbol{\Phi}^e\boldsymbol{P}^e(\boldsymbol{\Phi}^e)^{\mathrm{T}} + \boldsymbol{G}^eQ^e(\boldsymbol{G}^e)^{\mathrm{T}} - \hat{\boldsymbol{K}}^e(\boldsymbol{c}^e)^{\mathrm{T}}\boldsymbol{P}^e(\boldsymbol{\Phi}^e)^{\mathrm{T}} \tag{32a}$$

$$\hat{\boldsymbol{K}}^e = \boldsymbol{\Phi}^e\boldsymbol{P}^e\boldsymbol{c}^e\left((\boldsymbol{c}^e)^{\mathrm{T}}\boldsymbol{P}^e\boldsymbol{c}^e + R^e\right)^{-1}. \tag{32b}$$

The parameters Q^e and R^e serve as tuning factors for the estimator.

Controller. For the controller design, consider the disturbance-free error system

$$\boldsymbol{h}_{k+1}^{\mathrm{fb}} = \boldsymbol{\Phi}\boldsymbol{h}_k^{\mathrm{fb}} + \boldsymbol{\Gamma}u_k^{\mathrm{fb}} \tag{33a}$$

$$y_k^{\mathrm{fb}} = \boldsymbol{c}^{\mathrm{T}}\boldsymbol{h}_k^{\mathrm{fb}}. \tag{33b}$$

A steady-state LQR with disturbance feedforward

$$u_k^{\mathrm{fb}} = \boldsymbol{K}^{\mathrm{T}}\hat{\boldsymbol{h}}_k^{\mathrm{fb}} + \hat{P}_k^l \tag{34}$$

is designed, where the FB gain $\boldsymbol{K}$ satisfies the algebraic Riccati equation

$$\boldsymbol{P} = \boldsymbol{c}Q\boldsymbol{c}^{\mathrm{T}} + \boldsymbol{\Phi}^{\mathrm{T}}\boldsymbol{P}\boldsymbol{\Phi} - \left(\boldsymbol{\Gamma}^{\mathrm{T}}\boldsymbol{P}\boldsymbol{\Phi}\right)^{\mathrm{T}}\boldsymbol{K}^{\mathrm{T}} \tag{35a}$$

$$\boldsymbol{K}^{\mathrm{T}} = -\left(R + \boldsymbol{\Gamma}^{\mathrm{T}}\boldsymbol{P}\boldsymbol{\Gamma}\right)^{-1}\boldsymbol{\Gamma}^{\mathrm{T}}\boldsymbol{P}\boldsymbol{\Phi}, \tag{35b}$$

with the positive tuning factors

$$Q = (1\mathrm{m^3\,J^{-1}})^2, \quad R = (3.16\times10^4\mathrm{W^{-1}})^2. \tag{36}$$

5. RESULTS

The proposed 2DOF controller was tested in simulations for the validated FE model from Section 2 as the plant. The COMSOL MULTIPHYSICS model was embedded in a MATLAB/SIMULINK model similar to (van Schijndel, 2014).

Test Scenario. In the considered test scenario, the air gap a^{g} used in the FE model varies in space and time according to

$$a^{\mathrm{g}}(x,t) = a_0^{\mathrm{g}} - \hat{a}^{\mathrm{g}}\cos\left(k^{\mathrm{g}}(x - v_xt)\right), \tag{37}$$

with the parameters a_0^{g}=7.5mm, $\hat{a}^{\mathrm{g}}$=5mm, k^{g}=$\frac{\pi}{2}\mathrm{m^{-1}}$. The desired output temperature T_d^{out} describes a transition from ambient temperature of 30°C to 300°C and then remains constant.

[2] Due to the distance Δl from the coil to the output temperature pyrometer, see Fig. 1, the output is delayed by a dead time of $m\Delta t$, with m=$\lceil\Delta l/(v_x\Delta t)\rceil$ and the ceiling operator $\lceil\cdot\rceil$.

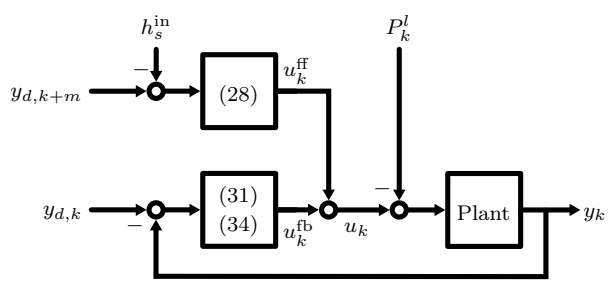

Fig. 4. 2DOF control structure with LQG controller.

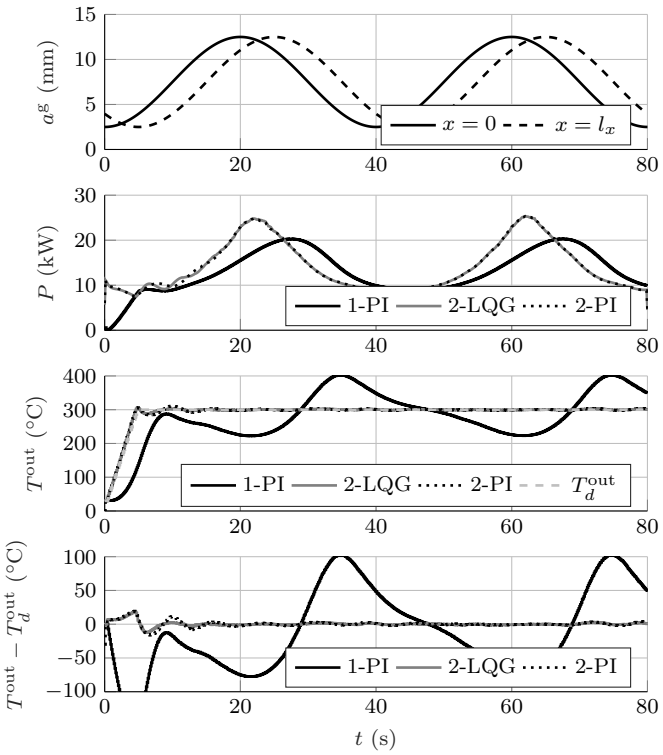

Fig. 5. Comparison of 1DOF PI (1-PI) to proposed 2DOF LQG (2-LQG) and 2DOF PI (2-PI) controllers.

Simulations. In the simulations, the 2DOF controller proposed in this paper is compared to two proportional-integral (PI) controllers. The first one is a naïve 1DOF PI controller tuned for the system (25) with R^c=0. The second one is a 2DOF PI controller. The PI part is derived from the proposed LQG controller by means of BALANCED TRUNCATION.

The results for all three controllers are depicted in Fig. 6. The proposed 2DOF controller meets the control goal, namely to keep the output error within the desired tolerance of ±50°C. Also, the reduced 2DOF PI controller produces very similar results. This shows that the FF branch of the proposed 2DOF controller and the introduction of the virtual input u_k are key components of this approach.

6. CONCLUSIONS

This paper demonstrates that induction heating of thin metal strips is subject to heavy disturbances from uncertain air gap geometries and that these disturbances can be efficiently compensated by a 2DOF control structure. A computationally expensive calculation of the electromagnetic field was avoided by employing an equivalent circuit model and the energy balance. Difficulties arising from nonlinear material parameters are circumvented by using the specific enthalpy as a system state instead of the temperature. Remaining model errors are captured by an estimated input disturbance, which is compensated by the FB controller. The resulting temperature controller is real-time capable and clearly outperforms the most commonly used 1DOF PI controller.

ACKNOWLEDGEMENTS

Excellent support by Plansee SE, especially by Michael Eidenberger-Schober and Gernot Reichl, is gratefully acknowledged.

REFERENCES

Canny, J. (1986). A computational approach to edge detection. *IEEE Transactions on pattern analysis and machine intelligence*, PAMI-8(6), 679–698.

Courant, R., Friedrichs, K., and Lewy, H. (1928). Über die partiellen differenzengleichungen der mathematischen physik. *Mathematische Annalen*, 100, 32–74.

Egalon, J., Caux, S., Maussion, P., and Pateau, O. (2012). Eigenvector placement in state space control of induction heating device. *IFAC Proceedings Volumes*, 45(21), 578–583.

Fujita, H. and Akagi, H. (1996). Pulse-density-modulated power control of a 4kw, 450khz voltage-source inverter for induction melting applications. *IEEE Transactions on Industry Applications*, 32(2), 279–286.

Gill, P.E., Murray, W., and Saunders, M.A. (2005). Snopt: An sqp algorithm for large-scale constrained optimization. *SIAM Review*, 47(1), 99–131.

Goodwin, G.C., Middleton, R.H., Seron, M.M., and Campos, B.J. (2013). Application of nonlinear model predictive control to an industrial induction heating furnace. *Annual Reviews in Control*, 37(2), 271–277.

Incropera, F.P., DeWitt, D.P., Bergman, T.L., and Lavine, A.S. (2007). *Fundamentals of Heat and Mass Transfer*. John Wiley & Sons, Hoboken, New Jersey, 6th edition.

Jackson, J.D. (2011). *Klassische Elektrodynamik*. De Gruyter, Berlin, Germany, 4th edition.

Jadachowski, L., Roetzer, F., Steinboeck, A., and Kugi, A. (2020). In-line estimation of the magnetization curve of steel strips in a continuous induction furnace. In *Proc. of the 21st IFAC World Congress*. IFAC, Berlin, Germany. Accepted.

Lucía, O., Maussion, P., Dede, E.J., and Burdío, J.M. (2014). Induction heating technology and its applications: past developments, current technology, and future challenges. *IEEE Transactions on Industrial Electronics*, 61(5), 2509–2520.

Ngoc, H.P., Fujita, H., Ozaki, K., and Uchida, N. (2011). Phase angle control of high-frequency resonant currents in a multiple inverter system for zone-control induction heating. *IEEE Transactions on Power Electronics*, 26(11), 3357–3366.

Nguyen, K.L., Caux, S., Kestelyn, X., Pateau, O., and Maussion, P. (2012). Resonant control of multi-phase induction heating systems. In *Proc. of the Annual Conf. IEEE Industrial Electronics Society*, 3293–3298. Montreal, Canada.

Park, N.J., Lee, D.Y., and Hyun, D.S. (2007). A power-control scheme with constant switching frequency in class-d inverter for induction-heating jar application. *IEEE Transactions on Industrial Electronics*, 54(3), 1252–1260.

Pham, H.N., Fujita, H., Ozaki, K., and Uchida, N. (2012). Estimating method of heat distribution using 3-d resistance matrix for zone-control induction heating systems. *IEEE Transactions on Power Electronics*, 27(7), 3374–3382.

Rhein, S. and Graichen, K. (2015). Dynamic optimization of induction heat-up and surface hardening processes on complex spatial domains. In *Proc. of the IEEE Conf. on Control Applications*, 1829–1834. Sydney, Australia.

van Schijndel, A.W.M. (2014). Implementation of comsol in simulink s-functions, revisited. In *Proc. of the 2014 COMSOL Conference*, 1–7. Cambridge, UK.

Zerad, J., Riachy, S., Toussaint, P., and Barbot, J.P. (2014). A nonlinear controller for parallel induction heating systems. *IFAC Proceedings Volumes*, 47(3), 11617–11622.